Exploration by Shake-the-Box technique of the 3D perturbation induced by a bubble rising in a thin-gap cell

Lucas Pavlov, Sébastien Cazin, Patricia Ern, Véronique Roig

Exploration by Shake-the-Box technique of the 3D perturbation induced by a bubble rising in a thin-gap cell

Lucas Pavlov[1,2] · Sébastien Cazin[2] · Patricia Ern[2] · Véronique Roig[2]

Abstract

From Lagrangian measurements using the Shake-the-Box technique (Schanz et al. in Exp Fluids 57(5):70, 2016) we investi-gate the velocity field about a single bubble rising in a thin-gap cell and we discuss it in an Eulerian framework of analysis. The gap thickness is equal to 2.85 mm and the bubble-induced perturbation extends over at least 10 cm in the plane of the cell, so that a very flat volume of observation is required. At first validation of the technique is provided during an emptying of the cell. It allows to fix all methodological parameters to ensure accurate measurements and, indirectly, to measure precisely the gap thickness. Then, the velocity field about a confined high-Reynolds number bubble is investigated. This velocity field is discussed in comparison with a previous description obtained by two-dimensional Particle Image Velocimetry (2D2C-PIV) with volume enlightening of the whole cell (Roig et al. in J Fluid Mech 707:444–466, 2012; Filella et al. in J Fluid Mech 778:60–88, 2015). Velocity is first averaged over the gap and compared to the 2D2C-PIV measurement obtained from tomo-reconstructed and projected frontal images. Then a 3D description of the velocity field is presented. It allows to discuss the quality and limitations of the 2D description of the wake with a velocity field integrated across the cell. In particular, the 3D description obtained from STB shows that the flow becomes mainly parallel to the cell plates at a distance of approximately one bubble diameter and that the wake is organised in slices parallel to the plates moving with their own dynamics that may vary their relative in-plane orientations, but all follow the general exponential viscous law of decay.

✉ Véronique Roig
roig@imft.fr

[1] Grupo de Medios Porosos, Facultad de Ingenieria, Universidad de Buenos Aires, CONICET, Paseo Colón 850, C1063ACV Buenos Aires, Argentina

[2] Institut de Mécanique des Fluides de Toulouse (IMFT), Université de Toulouse, CNRS, Toulouse, France

Graphic abstract

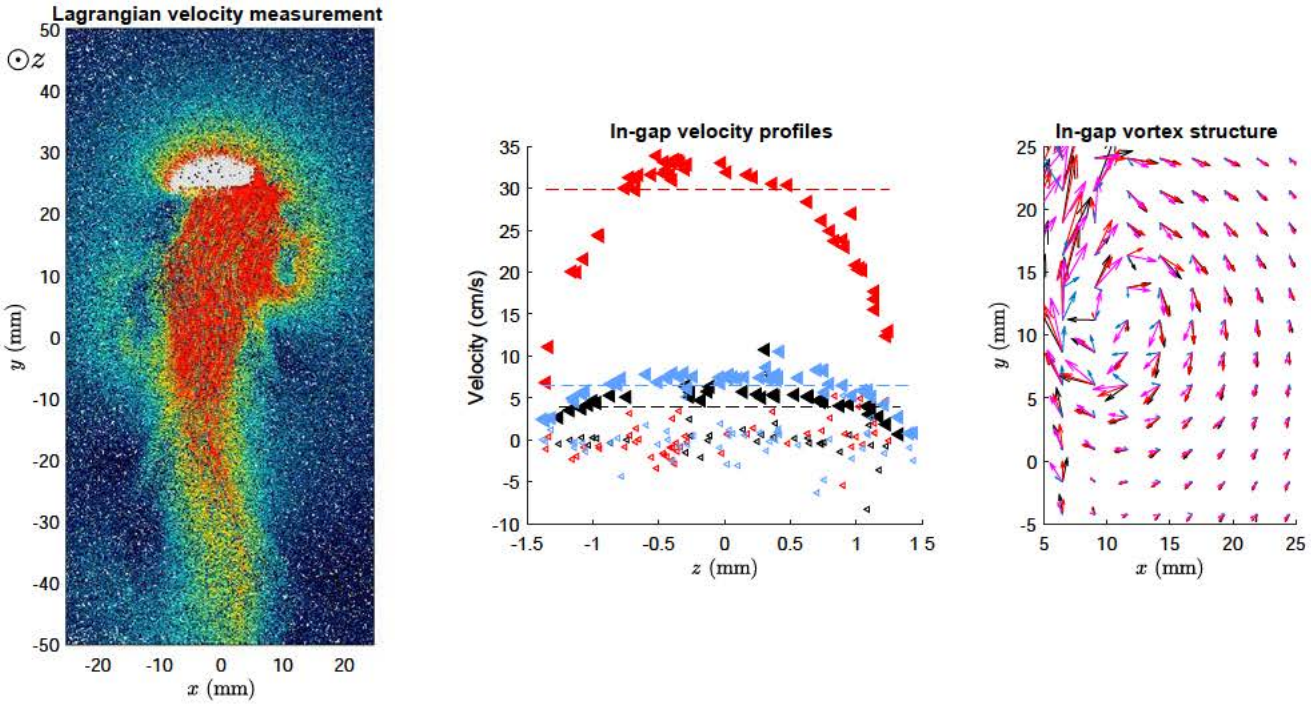

1 Introduction

The motion of single bubbles freely rising in a planar thin-gap cell filled with liquid, for bubble sizes larger than the gap-width—itself comparable to the capillary length—has been studied for several decades. Due to confinement the bubble is flattened between the two cell-plates. Inertial regimes with no de-wetting—that is where the bubble stays separated from the walls by thin liquid films—have been explored concerning in particular hydrodynamics (Collins 1965a, b; Lazarek and Littman 1974; Bessler and Littman 1987; Fan and Tsuchiya 1990; Bush and Eames 1998; Roig et al. 2012; Wang et al. 2014; Filella et al. 2015; Piedra et al. 2015; Wang et al. 2016; Hashida et al. 2019) or mass transfer (Roudet et al. 2017; Felis et al. 2019; Zhang et al. 2020). Indeed, this particular bubble flow configuration is relevant for fundamental investigation of a potentially interesting new bubble reactor configuration of intermediary size as compared to large bubble columns and small size monoliths flows.

For bubbles at high Reynolds number, typically higher than 500, several types of bubble motions exist as in unconfined flows, depending on the fluids properties and on the size of the bubble. As an example, large bubbles adopt a hemicylindrical cap shape and rise at a constant velocity associated with a straight path (Collins 1965a). In that case, the wake behind the bubble is closed and consists in attached counter-rotating vortices, which have been observed qualitatively many years ago (see for example Collins 1965b). More recently, deformable confined bubbles of intermediary size, with path and shape oscillations, have been studied experimentally (see Roig et al. 2012, Filella et al. 2015 and Hashida et al. 2019). In that case, vortex shedding occurs and the wake consists in a periodic vortex street of counter-rotating vortices. Roig et al. (2012) and Filella et al. (2015) studied quantitatively the velocity field in this wake using 2D-2C PIV with volume illumination integrated on a single frontal camera. The velocities obtained with this method were discussed as gap-averaged velocities. Indeed direct comparison of PIV measurements with interface displacement during an emptying of the cell validated this interpretation of the PIV measurement in specific flow conditions (see Roudet et al. 2011). However, those measurements do not give a description of the flow profile within the gap, which might depend on the distance to the bubble and may evolve with time. A full three dimensional (3D) description of the velocity field around such a bubble has never been reported. In recent numerical Volume Of Fluid (VOF) simulations, a two-dimensional (2D) approach was proposed to study the motion of confined bubbles (Wang et al. 2014, 2016).

In these studies the VOF momentum equation integrated a 'Hele-Shaw' sink term reproducing the shear stress at the walls. Thus, their predicted velocity field was the equivalent of a gap-averaged one under the hypothesis of Poiseuille flow within the gap. The goal of the present study is to obtain a 3D description of the velocity field about the bubble and to compare it with the 2D description existing in the literature. This will provide a deeper understanding of the strengths and limitations of the 2D approach, which is less complete but simpler to achieve. In addition, the knowledge of the flow profile within the gap could be useful to discuss 2D numerical models including walls effects.

The 3D velocity field can be measured from the images of tracer particles in a volume taken simultaneously from several cameras, using triangulation to obtain the particles' positions in space. This procedure requires a preliminary calibration using a three-dimensional target (Maas et al. 1993). Malik et al. (1993) developed such an approach to track individual particles in time, resulting in a Lagrangian description of the 3D velocity field (3D Particle Tracking Velocimetry (PTV)). With such a measurement method, the particle density must be low enough to avoid the presence of ghost particles (i.e. of particles found by triangulation but not corresponding to real particles) and allow particles recognition between two time steps. A different approach consists in obtaining an Eulerian description based on cross-correlation analysis of elementary volumes as in Tomographic Particle Image Velocimetry (Tomo PIV, see for instance Elsinga et al. 2006 and Scarano 2013). In that case, particles are not tracked individually but a greater particle density is necessary to validate measurements.

Recently, a high-density Lagrangian particle tracking method named Shake-the-Box (STB) has been developed (see Schanz et al. 2013b) and implemented in DaVis software from LaVision GmbH. This method allows to obtain particle trajectories resolved in time in three-dimensional space at high particle densities (typically 0.05 particles per pixel (ppp)) relying on an accurate iterative triangulation method (IPR, Wieneke 2013). The key point is that it takes advantage of the information of existing particle tracks to predict particle positions in the following time-step and uses this information to obtain an initial guess of the particle spatial distribution, that is afterwards refined to match the recorded images. New particles are detected by triangulation from the residual image of each camera that consists in the difference between the projected image from the reconstructed volume and the actual image. The residual images have a remarkably lower particle density than the original images and can thus be handled by standard triangulation techniques. A detailed description of the method, as well as a test on synthetic and experimental velocity fields, is given in Schanz et al. (2016), where the technique is successfully applied to synthetic images with particle densities up to 0.125 ppp in the case of noise-free images and 0.075 ppp when noise is added, and also in experiments with a particle density of 0.05 ppp. A critical requirement for the method to give accurate results is to have a calibration of high precision. The calibration procedure consists in taking one image of a three-dimensional calibration target (or several images of a two-dimensional target successively positioned at different known positions in space). Then, the information of the calibration target provides a mapping from the world planes coordinates to the camera sensor coordinates for all cameras. To this end, a pinhole model or a polynomial based one (see Soloff et al. 1997) might be used, the latter having the advantage of automatically taking into account the refraction of light rays through the different media that might be present between the calibration target and the cameras (for example, the fluid and the walls of the container). On the other hand, the polynomial method requires the calibration target to span a large part of the field of view of the cameras, which can be critical for confined systems. In general, sub-pixel accuracy is required (typically lower than 0.1 pixel) since the reconstruction method relies on triangulation from the images of pixel-sized particles in several cameras. Usually the quality of the calibration using the target is not good enough; in that case, a volume self-calibration (Wieneke 2008) using several images of the tracers is used to improve the quality of the mapping. This procedure has also the advantage that, after performing the self-calibration, the Optical Transfer Function (OTF) can be calculated from the particles' images (see Schanz et al. 2013a). This is important as the OTF characterizes the shapes of the particles' images in different regions of the observation volume as viewed by the different cameras. Those shapes, depending on the nature and geometry of the different mediums between the particles and the cameras (multiple refractions and associated optical aberrations), are essential for particle tracking purposes. Indeed, the knowledge of the OTF helps to improve the reconstruction from the cameras' images (Wieneke 2013).

In the present study we performed STB Lagrangian tracking of the flow surrounding a single confined high-Re bubble. In order to capture the bubble-induced velocity perturbation expanding over a large region of the cell plane, we explore a measurement volume that is strongly anisotropic, thin as the cell gap and large in both other directions. Typically the volume of observation is $64 \times 107 \times 3\text{mm}^3$. For data processing we used DaVis software. Difficulties consist in performing an accurate calibration and in measuring all the velocity components, all across the gap, in a flow configuration expected to be parallel to the walls except near the bubble.

The structure of the paper is as follows. In Sect. 2 the experimental setup, the calibration procedure and the parameters regarding the Shake-the-Box calculation are described. In Sect. 3 a validation of the STB technique is presented.

The velocity profiles obtained when the cell is slowly emptying are compared with the parabolic profiles expected at sufficiently long times, and to a theoretical solution valid for the transient regime (presented in the Appendix). This validation is also used to characterize the cell gap-widths (z-direction). In Sect. 4, a description of the three-dimensional velocity field generated by a bubble displaying path and shape oscillations is provided. The section first includes a comparison of the velocity fields averaged over the gap obtained either by STB or by 2D2C-PIV applied to the (x, y)-plane projected images rebuilt from the full tomogram (Sect. 4.1). This allows us to discuss in particular the meaning and limitations of the 2D2C-PIV measurements when using volume illumination, and to conclude on the robustness of the flow dynamics described by both techniques. Then, Sect. 4.2 introduces a detailed discussion of the 3D velocity field. It reveals the strengths and limitations of a 2D characterization of the flow and sheds light on the departure of a 2D-integrated description of the flow from a 3D one. The z-component of the vorticity of the vortices released by the bubble is also carefully analyzed. Finally, Sect. 5 outlines the conclusions of the paper.

2 Experimental method

2.1 Experimental set-up

The experimental set-up is a narrow vertical cell made of two glass plates of thickness 8 mm separated by a distance $h \approx 3$ mm in the z direction. Its dimensions, in respectively x and y directions, are a width of 21 cm and a height of 30 cm (Fig. 1), direction y being the vertical direction. The cell is filled with a mixture of distilled water and tracers at ambient temperature. Single air bubbles are injected from a capillary tube located at the bottom centre of the cell. Air is fed with a syringe linked to the tube and actuated by hand. The syringe may also be disconnected to empty the cell. Four high speed cameras (Phantom VEO 640L) are placed on the same side of the cell in a squared configuration, each of them pointing at the plates with an angle of approximately 20° between the line of sight and the direction perpendicular to the cell plane. The lenses are rotated with respect to the cameras' sensors in order to have the whole cell plane in focus (Scheimpflug condition). The focal length of the lenses is 200 mm and the f-number is 8. A high-speed pulsed laser (Quantronix Darwin Duo; 2×20 mJ at 1 kHz) of wavelength 527 nm is used to illuminate the cell from the front. The Volume Optics Modules from LaVision, which consist in vertical and horizontal cylindrical lens combinations, are placed between the laser and the cell in order to have an homogeneous volume illumination of the whole field of view. The liquid phase is a solution of water and fluorescent encapsulated Rhodamine

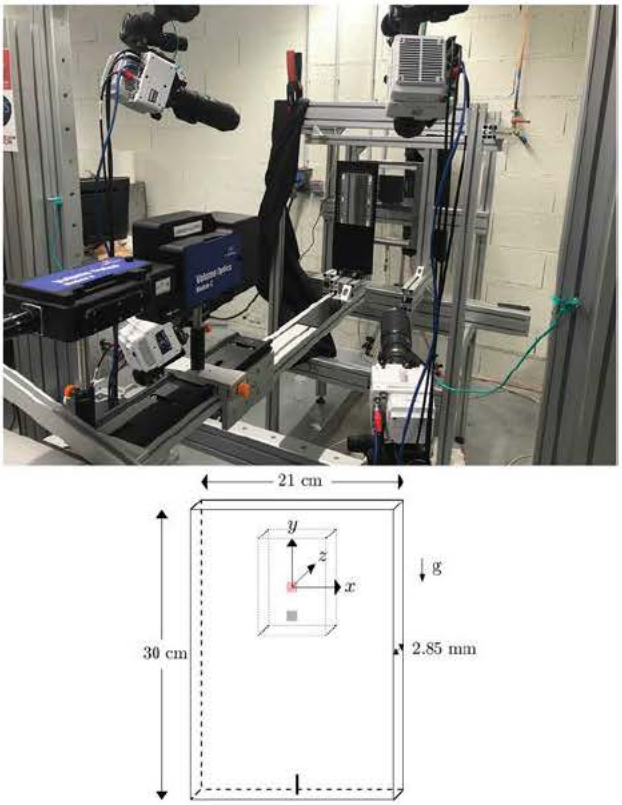

Fig. 1 Experimental setup. The four cameras and the laser can be seen pointing to the front part of the cell, which is open for calibration purposes. A closer view of the cell and the injection system can be seen in Fig. 2. The scheme on the bottom shows the definition of the axes and the region of measurement, as well as two regions (in red and grey) that will be used in Sect. 3

B particles with a median diameter of 21.4 µm and a density of 1030 kg/m^3. These particles absorb the light at the laser's wavelength and emit light with an emission peak at 568 nm. High-pass filters, 540 nm cutoff, are placed at the front of the cameras' lenses to avoid any laser light reflection on the bubble interface. Images of the particles are taken simultaneously by the four cameras at a frequency of 60 Hz when analyzing the emptying of the cell (Sect. 3) or 1400 Hz when performing experiments with bubbles (Sect. 4). The cameras' resolution is of 2560×1600 pixels. The volume that we investigate has the dimensions 64 mm $\times$ 107 mm $\times$ 3 mm and its centre is located at 22 cm above the bottom of the cell, where the bubble injection nozzle is positioned. It is highly non isotropic and measurements require an accurate calibration.

2.2 Methodology for calibration

In order to perform the calibration of the set of four cameras it is necessary to take an image of a calibration pattern placed in the measuring region with each of the cameras.

In the case of a thin-gap cell, the geometry of the device makes it difficult to place the calibration target inside the cell with precision (this problem also appears when dealing with microfluidic devices, see for example Hesseling et al. 2019).

To avoid this problem, a specific calibration procedure was followed. We used the 3D calibration plate 106-10 manufactured by LaVision, whose dimensions are 106 mm × 106 mm with two depth levels 2 mm apart, each one containing white dots of 2.2 mm diameter on a black background, with a distance of 10 mm between dots. A cell that can be disassembled and then reassembled was used. In order to perform the calibration, the back plate of the cell was removed and the calibration target was carefully placed against the front plate of the cell with a micrometric displacement system as shown in Fig. 2. A difficulty originates from the fact that the experiments are performed in water while there is air in the space between the two depth levels in the calibration plate when placed against the front plate. One possibility to deal with that could be to use a fictitious value for the depth of the calibration plate, that takes into account the difference in the refractive indices of water and air, when performing the calculations for the calibration (this procedure was followed in Hesseling et al. 2019). In our case, we filled with water the thin spaces between the deepest level of the calibration plate and the front glass plate. Finally, the calibration plate was removed and the back plate of the cell was carefully placed and adjusted, taking special care to avoid moving the front plate.

Calibration was then performed from the four images of the pattern using the software DaVis from LaVision (the same software was used for the Shake-the-Box calculation and for the tomographic reconstruction and PIV calculation of Sects. 2.3 and 2.4). A third order polynomial model coupled with an interpolation between the two world planes of the calibration target provided a mapping of the world volume coordinates to the camera sensors ones. Despite taking extreme care when closing the cell, a small disturbance in the position of the front plate is almost unavoidable. This would have negative effects on the results since a sub-pixel accuracy in the calibration is needed (Schanz et al. 2016). Therefore, a volume self-calibration (see Wieneke 2008) using pre-processed images of the tracer particles in the volume was performed independently on each recorded sequence. After a few iterations of the self-calibration procedure, the accuracy of the primary calibration was improved by one order of magnitude, passing from about 0.5 pixels to less than 0.05 pixels. In addition, the Optical Transfer Function (Schanz et al. 2013a) was calculated at the end of the self-calibration procedure, from the same set of images.

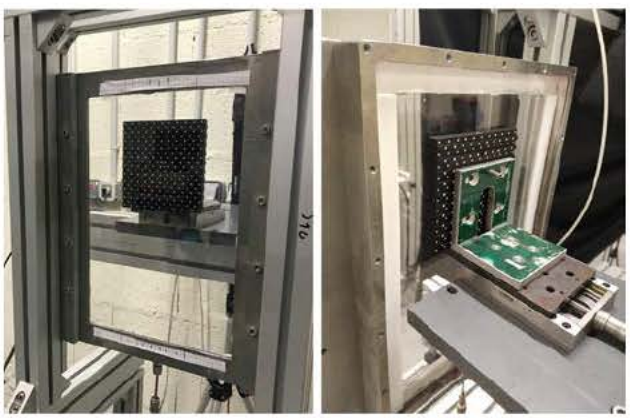

Fig. 2 Calibration plate placed behind the front plate of the cell. Near the centre of the calibration plate, a white square and a white triangle help to identify the orientation of the plate and the central white circle that will define the origin of coordinates

2.3 Shake-the-Box calculation

The Shake-the-Box calculation of the particles' trajectories is performed using images with the same preprocessing as in the self calibration and in the determination of the OTF. This is mandatory to ensure that the OTF correctly describes the particles' shapes in the images used for the STB calculation. A threshold for the detection of particles on each of the four images is set. An initial distribution of particles in space is obtained using the Iterative Particle Reconstruction method from the images of the four cameras. Particles' positions are shaked by 0.1 voxels in four iterations for each time step in order to improve their accuracy. In the first four time steps, a predictor based on a Tomo PIV analysis of the velocity field is used as a first guess of the particles' velocities in order to help in the identification of the first particle tracks. Particles that have a low intensity (lower than 10% of the average particle intensity) are removed. In the following time steps, the prediction of the particles' positions by extrapolation of their trajectories is used to speed up the particle reconstruction procedure (Schanz et al. 2016). In order to be accepted as valid, a given particle track must have a length of at least four time steps. In the tracking procedure maximum values for the particles' velocity and acceleration are set to reduce the search region around the predicted position, which reduces the computation time and the errors in particle identification in consecutive time steps. Those limits were set manually according to the maximum displacements of the particles in the measurement region. Finally, the results obtained for the positions for each particle track are fitted by a polynomial of order p for each time step t, considering to this end the positions of the particle from time step $t - L/2$ to time step $t + L/2$. We used $p = 2$ and $L = 5$ for the test case (Sect. 3) and $p = 3$ and $L = 7$ for the bubble (Sect. 4). In the present contribution, STB data are raw data. No filter, such as median filter, was applied to

them. This choice enables to evaluate the quality of STB measurements.

2.4 Technical tools for comparison with two-dimensional PIV

In this contribution, the results obtained with the Shake-the-Box method are compared with those obtained using the standard 2D2C-PIV technique applied to the frontal view of the reconstructed volume intensity. Therefore, first, the volume reconstruction is calculated for each time step from the images of the four cameras using the fast MART technique implemented in DaVis 10, that consists of a combination of the MLOS and SMART algorithms (Atkinson and Soria 2009) with intermediate volume smoothing (Discetti et al. 2013). The result is an intensity distribution of $1590 \times 2675 \times 88$ voxels that contains the whole cell gap. Then, the frontal projection of the tomographic reconstruction is obtained by summing the intensity of all the voxels along the gap, resulting in an image of 1590×2675 pixels in which the intensity of each pixel is the sum of the intensity of the 88 voxels that have the same (x, y) coordinates. This frontal projection is similar to the image that would have been recorded using a single camera equipped with a telecentric lens so that the reconstructed frontal view is not affected by parallax effects. Thus, the results obtained by applying the 2D2C-PIV technique to these images can be considered as similar to those that would have been obtained using a single frontal camera, as long as the number of ghost particles is not large enough to cause false correlation peaks. The two dimensional velocity field is obtained using the PIV technique with one initial pass with a window of 64×64 pixels followed by four passes at 32×32 pixels, with an overlap of 75%.

The PIV results will be compared with those from Shake-the-Box (Sect. 4.1). To this end, using an home-made Matlab code, an Eulerian description of the mean velocity field is obtained from the Lagrangian measurements by averaging the velocities of all particles inside adapted rectangular parallelepipeds that coincide with the PIV grid in the cell plane.

The frontal projection of the tomographic reconstruction is also useful to obtain the motion and shape of the bubble in a similar way as when performing shadowgraphy experiments using a backlight LED, although the result might be less accurate due to the presence of the particles in the vicinity of the bubble, which are sometimes stuck to the bubble's surface (specially in its rear part). An example of a frontal projection is shown in Fig. 3, together with the estimation of the bubble contour and with the particles tracked by the Shake-the-Box algorithm superposed to it, which show that more than 90% of the particles detected with the Shake-the-Box technique are in regions of high gray level intensity (which correspond to reconstructed particles with the fast MART technique). Conversely, there are almost no regions of high gray level without tracked particles, which confirms that the fraction of ghost particles in the tomographic reconstruction is low, since particles detected by the Shake-the-Box algorithm in the converged state can be regarded as true particles (Schanz et al. 2016).

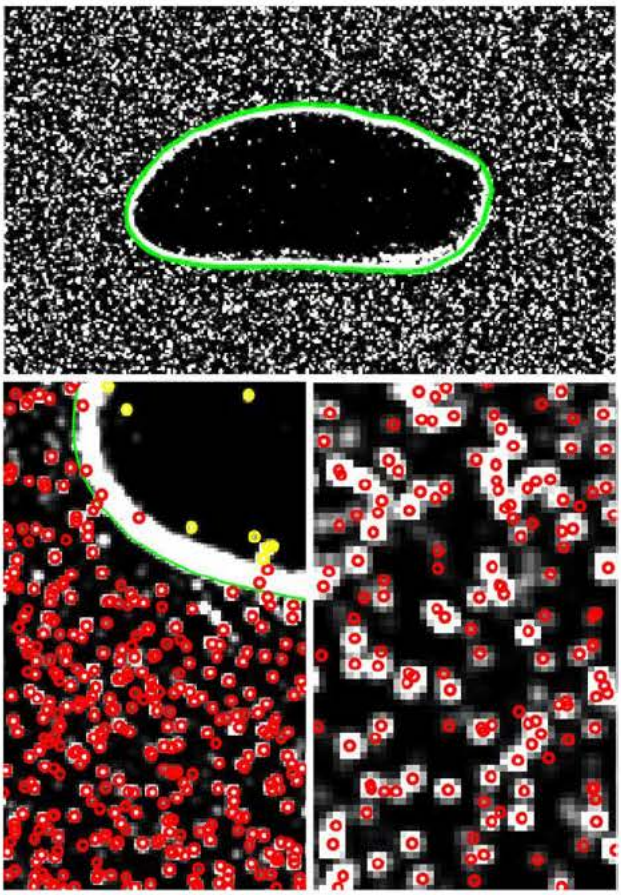

Fig. 3 Frontal projection of the reconstruction obtained with the fast MART algorithm and, in overlay, the positions of the particles detected with the Shake-the-Box technique. A linear contrast enhancement transformation was applied to improve the visibility of the particles. Top: bubble with the estimated contour (green line). Bottom left: zoom in the rear left part of the bubble; particles detected with the Shake-the-Box technique are shown in red, or yellow for the particles that are in the thin film between the bubble and the front plate of the cell, which were fixed in the laboratory frame while the bubble was rising; the particles behind the bubble, i.e. in the thin film located near the back plate, are not detected because the air bubble has a different refractive index than water, and therefore the particles behind it cannot be successfully reconstructed as the calibration was performed in a water medium. Bottom right: a closer view in the region of the wake

3 Validation of 3D velocity field measurements

The Shake-the-Box calculation was first applied to the emptying of the thin-gap cell initially filled with water at rest. This test allows us to discuss the methodology and the precision of measured velocities, as they can be compared to a theoretical solution. It also provides the spatial distribution of the thickness of the cell $h(x, y)$, which is in fact required for a sound characterization of the bubbles' dynamics, as any spatial inhomogeneity of the gap thickness could be expected to have an impact on the 3D character of the velocity field.

The region of observation was always kept far from the free surface, where tracers are not uniformly distributed. In particular, the dripping of the liquid films remaining on the cell walls after the passage of the free surface induces noticeable perturbations to the homogeneity of the tracers concentration and of the velocity field on length scales up to 10 mm.

A typical average density of the tracked particles as a function of z is plotted on Fig. 4a. This particle density was calculated in a region of 40 mm × 40 mm in the cell plane, and the particles were distributed in sets according to their position within the gap. Layers of 0.05 mm thickness in the gap direction were considered. The measured particle density was of the order of 6.4 particles/mm^3, considering only the tracked particles. This gives a density of 0.00041 tracked particles per voxel or 0.029 particles per pixel taking into account the gap width, which is within the accepted limits for the Shake-the-Box technique (Schanz et al. 2016).

Instantaneous particles distributions show that particles are always tracked all across the gap so that a measurement of the velocity profile in z-direction is possible. The region associated to positive values of z is the one nearest to the cameras. This can explain that particles are slightly more easily tracked on this side because they are submitted to less occultations. Deviations from uniformity in the particle density are not a problem for a Lagrangian scan of the velocity field, but could have an impact on the Eulerian re-projection of the velocities. In the present conditions, the z-profile of the average density of particles is not so far from uniform (Fig. 4a), allowing a correct re-projection. The velocities averaged across the gap obtained from the Shake-the-Box analysis can then be compared with the free surface velocity, which is a direct measurement of the gap-averaged velocity of the fluid. The air-water level position was tracked with sub-pixel accuracy from the front view of the tomographic reconstruction of the cell applying a detection on grey levels and the interface velocity was obtained by discrete differentiation. Within the

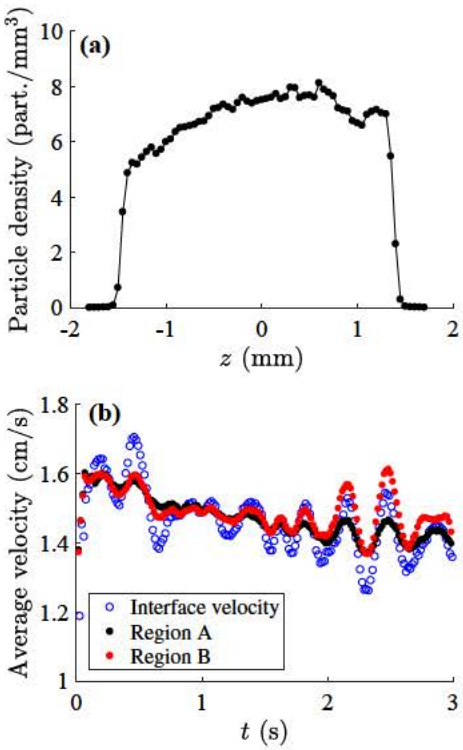

Fig. 4 **a** Distribution of tracked particles across the gap. (A constant value was subtracted to the original z values in order to locate the cell centre at approximately $z = 0$ plane. The precise cell centre in z-direction is obtained afterwards from fits of the velocity profiles. This average particle density was calculated over a time interval of 1.7 s and in a squared central region of the cell of size equal to 40 mm.). **b** Temporal evolution of the gap-averaged vertical velocities V. (The gap-averaged velocities are also averaged over particular (x, y) regions of the cell far from the interface. Regions A and B are squares of extension 10 mm x 10 mm in the cell plane, and are located in the centre of the cell in the x-direction. The centre of region B is 25 mm above the centre of region A. These regions are represented in color in the bottom part of Fig. 1

measurement time, the free surface velocity U decreased in between 16 and 13.5 mm/s due to a decreasing water level. This can be seen in Fig. 4b. The same figure reveals oscillations of the flow that may be generated at the outlet boundary condition and shows that the STB analysis leads to a similar gap-averaged velocity that follows the same oscillations, wherever it is measured.

Discarding these oscillations of moderate amplitude, during the present short period of exploration, the emptying can be seen as an unsteady laminar flow developing from uniform to Poiseuille profile with a constant flow rate. In fact, the Reynolds number evolves from 45 to 40, and as the mean velocity changes only weakly due to the moderate change in free surface level, the emptying can be assumed as being at nearly constant flow rate. Under such hypothesis, an analytical solution of the temporal development of the profile in the z-direction of the vertical velocity $V(z, t)$ can be

found. It is reported in Appendix A (relation 5). It is written as a series that reproduces the development from plug-like to Poiseuille profile. At each time step, the velocity profile can also be fitted by the simpler relation

$$v(z) = \bar{V}\frac{\beta+1}{\beta}\left(1 - \left|\frac{2(z-z_c)}{h}\right|^{\beta}\right), \quad (1)$$

where z_c is the location of the centre of the channel, h its width, $\bar{V}$ the averaged velocity and β a coefficient that characterizes the shape of the profile, being equal to 2 for Poiseuille flow.

These parameters were determined by a non linear regression from the downward velocities measured by STB for each element (2 mm × 2 mm) of a grid meshing the (x, y) plane. In Fig. 5a the temporal evolution of the velocity profile from plug-like to Poiseuille law obtained from the measurements is reported. It is correctly reproduced by relation (1) with a power exponent β that evolves with time as reported in the subplot. When the analytical solution reported in Appendix A is fitted by relation (1) for an average velocity equal to that of the experiments, the power exponent follows the same decrease with time (black line in subset in Fig. 5a). This shows that the physics of emptying are correctly and very precisely measured. Moreover, Fig. 5b shows the spatial distribution of the gap-width h obtained by the regressions of the velocity profiles. This indirect measurement of h shows that the gap-thickness slightly varies in space, its mean value being $h = 2.85$ mm with variations in the range [2.82, 2.90] mm. This is consistent with the mean gap thickness that can be inferred from the profile of the particle density within the gap (Fig. 4a).

All these results show that, despite the marked flatness of the volume of measurement, the STB methodology is accurate enough to investigate the 3D velocity field inside the cell.

4 Three-dimensional velocity field induced by an oscillating confined bubble

We now focus on the flow perturbation induced by an inertial single bubble confined in the cell and rising freely in the liquid otherwise at rest. We consider the case of an elongated bubble displaying path and shape oscillations (see Fig. 11a) coupled to the unsteady wake. The bubble is characterized by the equivalent diameter $d = 8.9$ mm associated with its projected area S on the cell plane ($S = \pi d^2/4$, the volume of the bubble being $\approx Sh$), and it is thus flattened in the gap ($h/d = 0.32$). The Archimedes number is $Ar = \sqrt{gd}d/\nu = 2620$ and the Bond number $Bo = \rho g d^2/\sigma = 10.5$ (g being the gravitational acceleration and σ the water-air interfacial tension). The path and shape

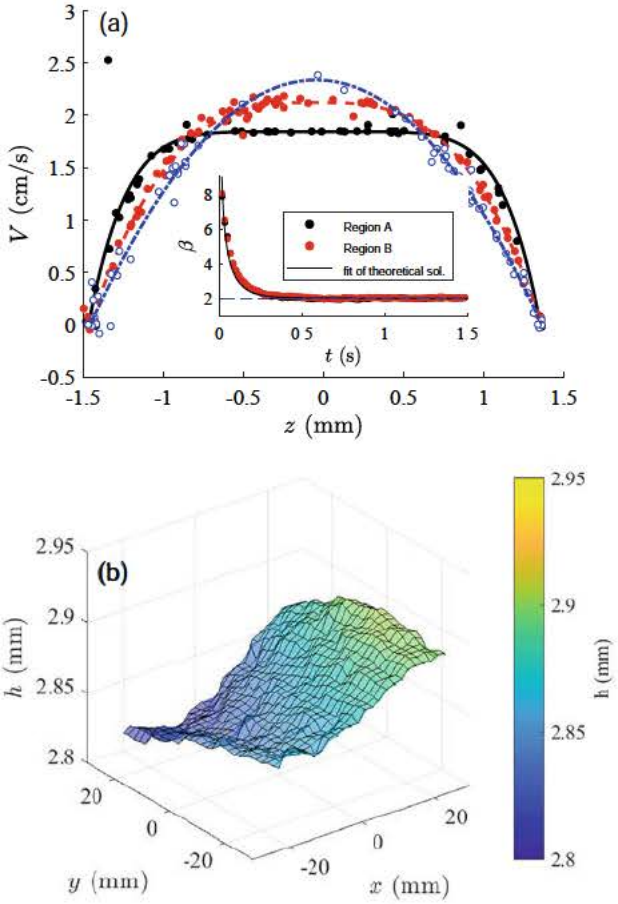

Fig. 5 **a** Temporal evolution of the in-gap downward velocity profiles. Velocities are picked up in a region of 2 mm×2 mm in the (x, y) plane centred at $x = -0.69$ mm, $y = 26.4$ mm. Dots are experimental STB measurements (each dot represents the downward velocity of a tracked particle in the given region), lines are the velocity fits by relation (1). The various colors indicate different times during emptying experiment: black $t = 0.0533$ s ($\beta = 6.22$), red $t = 0.137$ s ($\beta = 3$), blue $t = 0.737$ s ($\beta = 2$). Subplot shows the temporal evolution of the exponent β of the law used for the velocity fit. Once calculated from the fit of the experimental data with relation 1, it has been averaged over region A or B (black and red dots) defined in Fig. 4. Another value of β has also been extracted from a fit by relation (1) of the theoretical solution consisting in the series provided by relation (5) (black line). **b** Spatial distribution in the (x, y) plane of the width h of the gap. It has been measured from the fit by relation (1) of the velocity distributions across the gap for different regions in the (x, y) plane

of the bubble have been measured from tomographic reconstructed front views. The shape elongation ratio χ—defined as the ratio of the major and minor axis lengths, in (x, y) plane, of the ellipse that has the same normalized second central moments as the bubble—varies in between about 2.5 and 3.5 and has a mean value equal to 2.8. The mean rise velocity of the bubble V_∞ is equal to 19.8 cm/s, and its period of oscillation T is equal to 0.23 s. The sampling frequency chosen for the investigation was thus set to 1400 Hz. The density of tracked particles in this experiment was of

approximately 12 particles per mm^3 corresponding to 0.058 tracked particles per pixel which is again within the accepted limits of the STB technique (Schanz et al. 2016). A comparison of the kinematics of this bubble with the scaling laws introduced for this range of non-dimensional numbers by Filella et al. (2015) shows good agreement, even if the extension of the cell plane is reduced in the present study. Indeed V_∞ is 7% higher than the predicted terminal velocity and the mean value of χ is 12% higher than the predicted value but they are within the limits of data scattering. The amplitudes of the shape and path oscillations are also comparable to those measured by Filella et al. (2015) under data scattering.

Up to now, the 3D structure of the flow around the confined bubble has never been explored. The perturbation induced in the liquid has been characterized by the 2D2C-PIV technique using a camera placed in front of the cell and volume enlightening of the cell. This technique provided a measurement of the velocity of the liquid discussed as being averaged over the gap width h (Roudet et al. 2011). Despite its limitations, the technique revealed the strong exponential attenuation of the wake due to confinement and the associated specific dynamics of the vortex street (Roig et al. 2012; Filella et al. 2015). In this section, STB velocity measurements are first analyzed to estimate a gap-averaged velocity field. This allows a direct comparison with the velocity field obtained from 2D2C-PIV applied to reconstructed front views. We will therefore discuss precisely the robustness of PIV measurements that have been performed up to now and that are still much easier to perform. Then, we will use STB velocity measurements to explore the 3D structure of the flow. We will also discuss the limitations of the measurements resulting from the strong contrast between in-plane velocities and the z-component of velocity.

4.1 Discussion of the flow around the confined bubble with velocities averaged through the gap

We first discuss a comparison between (1) an Eulerian velocity field obtained with the 2D2C-PIV technique and (2) the reprojection on an Eulerian grid of the Shake-the-Box Lagrangian measurements of particle velocities that are averaged through the gap. 2D2C-PIV is performed on projected images reconstructed from the tomogram. In this discussion we consider velocity vectors reduced to x- and y-components. This first part allows to discuss the quality of a flow characterization using a gap-averaged measurement of the velocity. It also helps to check the quality of the reprojection of STB information on an Eulerian grid, which is used for vorticity measurements.

2D2C-PIV calculation was performed on the tomo-reconstructed frontal images with a window size length $dx = dy = 1.286$ mm (see Sect. 2.4). The STB reprojection was achieved on exactly the same (x, y) grid and, for each grid element, it provides an average velocity of all the particles distributed across the whole gap whose (x, y) positions are inside the grid element. The tracers seeding ensured on average 48 particles per grid element with a very small variation as the *rms* value of the number of particles per element was 7.

4.1.1 Respective meaning of the velocity obtained by volume-illuminated 2D2C-PIV and of the gap-averaged velocity obtained by the STB technique

When calculating a gap-averaged velocity $\mathbf{V}_{STB}$ from the STB technique or when measuring by volume-illuminated 2D2C-PIV a velocity $\mathbf{V}_{PIV}$ as in Filella et al. (2015), it is evident that both types of measured velocities depend on the particle distribution across the gap as there are large velocity gradients in the gap direction. But for a uniform distribution of tracers across the gap, as it is the case in our measurements (see Fig. 4), the gap-averaged velocity $\mathbf{V}_{STB}$ obtained from STB technique is unambiguously defined and meaningful. For uniform distributions of tracers, mean velocity obtained from 2D2C-PIV is nevertheless still ambiguous due to the large velocity gradients through the gap. Indeed, tracers have different velocities depending on their positions within the gap, and, as a consequence, the shape of the displacement correlation peak is expected to be broad. It can be thus difficult to find a clear maximum of the correlation, and even if it is possible, the meaning of the associated velocity $\mathbf{V}_{PIV}$ as a gap-averaged one is not obvious *a priori*. This is why Roudet et al. (2011) had to check *in situ* under which conditions the PIV measurement could be associated to a gap-averaged velocity before exploring confined bubble wakes. In the present contribution, we provide a direct comparison of both types of velocity measurements starting with the examination in Fig. 6 of the displacement correlation obtained by PIV. For simplicity, we use in this figure experimental data from the experiment of cell emptying. In this configuration, tracers have the same vertical descending direction whatever their positions through the gap, and the true gap-averaged velocity is known from the motion of the gas–liquid interface (blue dashed line in the figure). Two 2D2C-PIV velocities are calculated from two different frontal views obtained by tomographic reconstruction of the particle distribution. One is calculated from the particles in the whole gap volume and we can consider that it is representative of an attempt to measure the gap-averaged velocity. The other frontal view is reconstructed from particles that are in a layer of 1 mm thickness in the centre of the gap where the flow is uniform. It is interesting to compare the shapes of the correlation peak. A contrast transformation

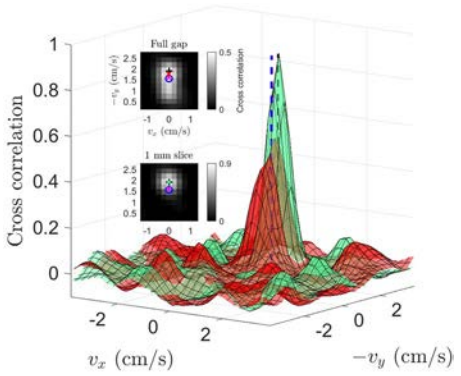

Fig. 6 Example of a correlation peak between consecutive images at the beginning of the emptying. Red (resp. light green) corresponds to the frontal view of the tomographic reconstruction of the full gap (resp. centered layer of 1 mm thickness). A 2D view in grey level intensity of the region near the peak is also provided in the inserts. The axes were scaled using the spatial and temporal resolution to reflect velocities instead of pixel displacements. The dashed vertical lines (or symbols in the 2D representations) correspond to the maximum velocity from the STB profile (black line/+ symbol), to the average velocity from the STB profile (magenta line/x symbol) and to the average velocity from differentiation of the gas–liquid front position (blue line/empty circle). The red or light green crosses in the 2D representations correspond to the positions of the correlation peaks calculated with sub-pixel accuracy using a Gaussian peak fitting

was applied to the tomographic reconstructed and projected raw images in order to have all particles at similar intensities. This is necessary because, otherwise, brighter particles would dominate the cross-correlation, and since different particles have different velocities depending on their position within the gap, this would result in a noisy velocity field dominated at each grid element by the velocities of the brightest particles. The correlation peaks are shown in Fig. 6 in a square of 64×64 pix centred at $(x, y) = (7.85$ mm, -14.2 mm) at the beginning of the emptying (between the images at $t_1 = 0.053$ s and $t_2 = 0.070$ s). The results are compared with the mean downward velocity measured from the front positions between those two instants, and with the maximum and average downward velocities obtained with the STB measurement in the same region for the same time interval.

It is clear that the gap-averaged velocity obtained by the STB technique (plotted in magenta) is very similar to the velocity of the gas–liquid interface (in blue). This measurement of a gap-averaged velocity is robust due to the homogeneous distribution of tracers. The PIV correlation peak associated to the 1 mm centred layer is plotted in green color. At the time of measurement, the velocity profile in the 1 mm centred layer can be regarded as uniform (see Fig. 5a). The correlation peak is thus also well-defined, symmetrical, and, as expected, the measured velocity using the 2D2C-PIV technique agrees with the maximum velocity measured by STB (plotted as a black vertical dashed line). On the contrary, the correlation peak associated to the full gap (plotted in red color) is quite elongated in the y-direction of the motion. This is the signature of the presence of contrasted y-components of the velocity in the region of PIV interrogation. As can be observed in particular in the insert, the position of the maximum of correlation (red cross) provides a velocity higher than the true gap-averaged velocity plotted as a blue empty circle. The difference between $\mathbf{V}_{PIV}$ and $\mathbf{V}_{STB}$ was observed to vary randomly with the position in the cell. This may be understood as due to the sensitivity to noise of the localisation of the maximum of correlation for broad peaks.

Those results confirm that the gap-averaged velocity measured by STB technique is robust and that volume-enlightened PIV measurement provides a more ambiguous velocity measurement, as it leads to widespread correlation peaks in the presence of particles moving at different velocities in the same interrogation region.

In the following, a quantitative and statistical comparison of the velocity field obtained by 2D2C-PIV with the gap-averaged velocity field obtained by the STB technique is provided for the motion generated by a confined bubble. It will show that, despite the more ambiguous meaning of the PIV measurement, 2D2C-PIV technique and STB technique both provide dynamical descriptions of the flow that are in rather good agreement and that are also in agreement with previous measurements (Roig et al. 2012; Filella et al. 2015).

4.1.2 Comparison of averaged velocity fields past the bubble issued from the STB and 2D2C-PIV methods

Figure 7 presents the comparison of both instantaneous velocity fields.

At first glance, on Fig. 7a, both fields look alike. The evolution along the three lines plotted on the velocity field (respectively in red, light blue and black colors) of the norm of the velocity vector $|V|$ and of its orientation θ with respect to the ascending vertical direction are reported in Fig. 7b. A closer examination of these profiles obtained either from STB reprojection or from 2D2C-PIV measurements shows that they are both nearly identical. The flow consists in a potential flow in front of the bubble and in a rapidly dampened wake downstream, as already observed in Roig et al. (2012) and Filella et al. (2015). At the given time of observation, the potential flow in front of the bubble is nearly symmetrical (profiles along the light blue line) and the flow in front of the bubble, as well as in the wake, is nearly vertical (profiles along the red line). In the wake, along the transverse black line, STB or PIV measurements are closely superposed and reveal a steep velocity profile that can be explained by the negligible in-plane momentum diffusion.

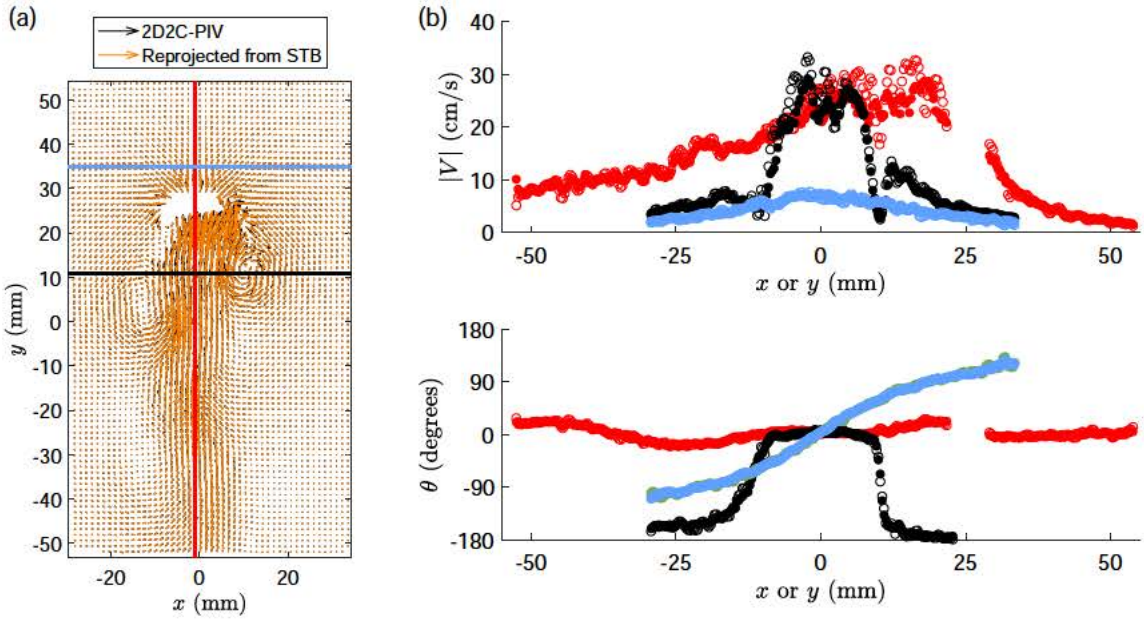

Fig. 7 **a** Comparison of 2D2C-PIV and STB measured velocity fields at a given time step, **b** norm and angle of inclination of the in-plane velocity vectors as a function of x for the transverse profiles (respectively, y for the longitudinal one) along the colored lines plotted in (**a**): filled circles for STB reprojection, empty circles for 2D2C-PIV estimations. The reader is referred to the video provided as supplementary material for a time-resolved Lagrangian description of the velocity

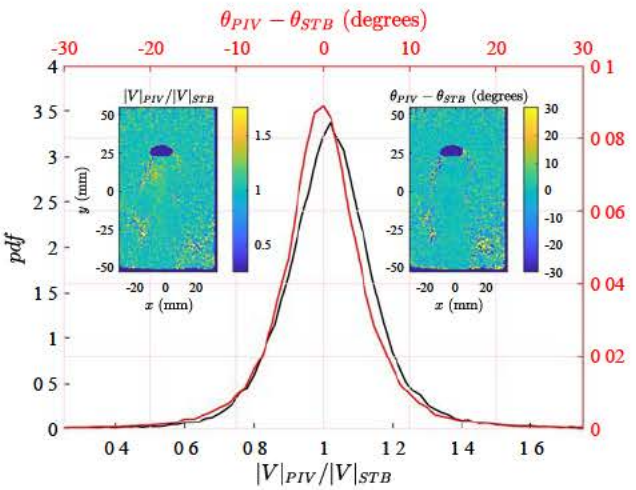

Fig. 8 Statistical comparison of 2D2C-PIV and STB measured velocity fields (events are taken from the whole field at $t = 0.6$ s)

The most noticeable difference between the 2D2C-PIV and STB measurements is that the 2D2C-PIV measurement leads to a noisier velocity field, in particular in the near-wake where 3D structures are present. To get a deeper comparison, the ratio of the absolute values of the in-plane velocity vectors obtained from both techniques $\frac{|V|_{PIV}}{|V|_{STB}}$ and the differences between orientations $(\theta_{PIV} - \theta_{STB})$ were computed for each grid element, and a statistical analysis that takes into account all the elements of the grid was performed. The probability density functions of both parameters measured for the whole field at a single time step are reported in Fig. 8. They reveal that both measurements of the gap-averaged velocity are very similar. Indeed, the *pdf* of the velocity ratio is centered on the value 1.02 and has a small *rms* value of 0.15. Similarly, the *pdf* of the difference of orientations is centered on zero and has a moderate *rms* value of 8.6 degrees. For the velocity intensity and orientation, the most important differences between both measurements are observed in the same regions located at the borders of the wake (inserts of Fig. 8). They are linked to localized stronger velocity gradients, that are poorly captured by the 2D2C-PIV method as they result in broad correlation peaks, the STB providing the real gap-averaged velocity. Finally, we may, however, retain that both measurements validate themselves.

In order to examine even further the comparison between measurements by 2D2C-PIV and STB techniques, it is interesting to compare fluid dynamics quantities that can be deduced from the velocity fields. For an unstable confined bubble, the dynamics of the wake has been characterized in previous works by two major features: the non-material line of maximal velocity in the wake and the released vorticity. They have been obtained up to now by 2D2C-PIV measurements (Filella et al. 2015) and proved to be pertinent to model bubble–bubble interactions (Filella et al. 2020). At a given time step t, the spatial evolution of the ascending

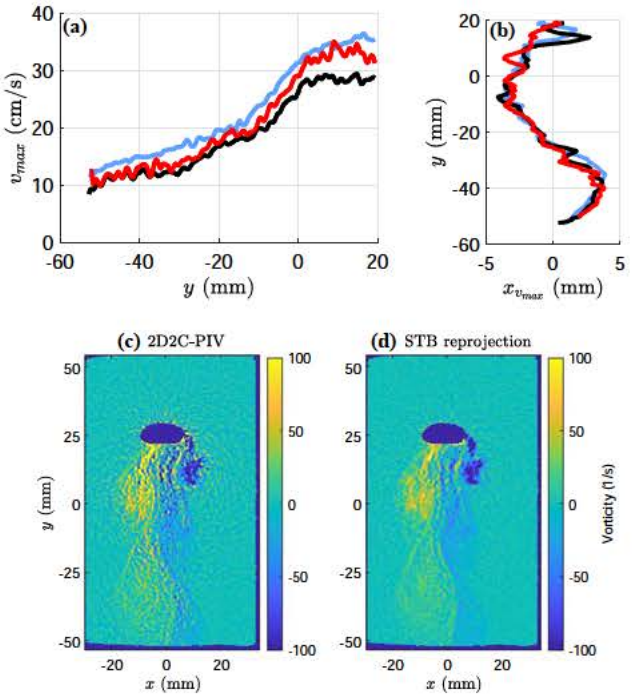

Fig. 9 Consistency of wake characterization using velocities averaged through the gap obtained from the STB reprojection (black line) and from 2D2C-PIV measurements using the front projections of the tomographic reconstruction (red line). **a** Longitudinal evolution of the norm $v_{\max}$, **b** position of the line where $v_{\max}$ is detected, **c** vorticity field obtained from 2D2C-PIV measurements, **d** vorticity field obtained from STB reprojection. (in **a** and **b** light blue lines represent the measurements from the STB reprojection using only a central slice of thickness $\delta z = 0.4$ mm)

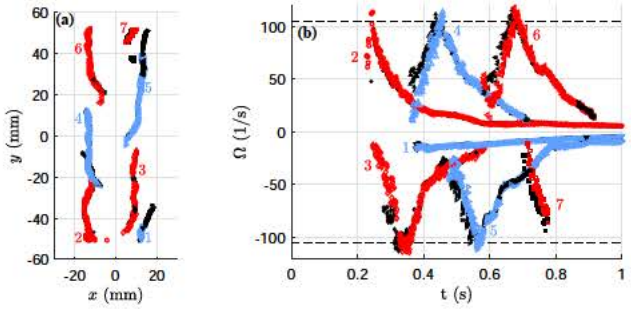

Fig. 10 Released vortex characterization from velocities averaged through the gap obtained either from 2D2C-PIV measurements or STB reprojection. **a** Trajectories of the released vortices, **b** temporal evolution of the vorticity of the released vortices. Black filled symbols: STB, red or light blue open symbols: PIV, dashed line is the value provided by the scaling law for Ω_0 from Filella et al. (2015). Vortices were numbered following the order of release from the bubble surface. Only 3 vortices were tracked for sufficiently long times as to finally reach a fixed position

flow behind the bubble can be characterized by the position $x_{v_{\max}}(y,t)$ corresponding to the maximal value $v_{\max}$ of the norm of the liquid velocity for each longitudinal position y. In Fig. 9a and b the $v_{\max}$ values and the positions $x_{v_{\max}}$ extracted from both measurements are shown to be similar except near the bubble. This indicates the robustness of the characterization of the vertical entrainment in the wake by STB calculation (black symbols) as compared to 2D2C-PIV measurements (red symbols). In the region located near the bubble interface the flow is strongly 3D and the PIV overestimates $v_{\max}$ as compared to the STB reprojection. The positions of the lines of maximal velocity also differ. But, at larger distances from the bubble, the exponential decrease of the maximum velocity and the unsteady sinuous behaviour of the line of maximal velocity are retrieved by both methods as in Filella et al. (2015). The vorticity fields are also compared in Fig. 9c. Vorticity is calculated from the 2D velocity field using a least squares scheme (Adrian and Westerweel 2011). It can be noticed that both vorticity fields have a similar spatial distribution and a similar range of intensity. Both vorticity fields illustrate the rapid attenuation of the vortex street due to the shear stress at the walls. But interestingly, vorticity estimated from the STB reprojection is more continuous and less noisy than the one obtained from PIV, similarly to velocity measurements. Finally, vortices released in the wake of the bubble have been identified and characterized by their time evolving position and vorticity (Fig. 10). Their detection is based on the Γ_1 vortex identification function (Graftieaux et al. 2001) using a threshold value of 0.55. Their vorticity $\Omega(t)$ is defined at a given time step as the average of the vorticity values in the region of the flow where $|\Gamma_1|$ is above the threshold. Figure 10a and b show that, for 2D2C-PIV and STB measurements, the paths followed by the released vortices are superposed and that their vorticity is neither dependent on the method of measurement, except at early stages where a small delay is observed (the maximum vorticity is achieved a bit earlier for the STB reprojected measurement); this difference might be explained by the velocity field dependence on z, which is important at early stages in the vortical regions as will be shown later (in Fig. 13). The vortices have a finite path due to the attenuation of their motion by the confinement (Fig. 10a). Figure 10b reveals the regular behavior of their vorticity that first increases towards a maximum value similar to that, $\Omega_0 = V_\infty \chi^{3/2}/d$, observed by Filella et al. (2015), then decreases due to vortex interaction and, later on, decreases far more slowly due to friction at the walls. The period of vortex release determined from the time delay between the maxima of vorticity is identical to the period of the bubble path due to the coupling between the bubble motion and its wake.

As a conclusion for this comparison, the dynamics discussed on the basis of the liquid velocity averaged through the gap is not sensitive to the method of measurement by STB or volume-illuminated 2D2C-PIV except near the bubble, at a distance less than $2d$. It remains that such a

description of the perturbation induced in the flow using a gap-averaged velocity only provides an averaged view of the flow. Questions remain that will be explored in the following: is the flow 3D? Is it parallel to the planes of the cell, at least far from the bubble? What are the velocity profiles in the z-direction? Is the z-component of vorticity extracted from gap-averaged measurements of velocity representative of a gap-averaged value of the z-component of vorticity?

4.2 Velocities distributions across the gap obtained by STB

From the STB method, unsteady and three-dimensional particle trajectories and velocities were obtained as illustrated in the movie provided as supplementary material. We now present the exploration of the flow from these data in an Eulerian framework of analysis.

Figure 11 shows instantaneous velocity profiles in the gap (z-direction) measured upstream and just downstream of the bubble for the six locations at $y = 35$ and 19.9 mm indicated in Fig. 11a. The norm of the in-plane vector $\mathbf{V}_{2D}(x, y, z, t) = v_x\mathbf{e_x} + v_y\mathbf{e_y}$ and the z-component v_z are reported on Fig. 11b (where $\mathbf{e_i}$ are unit vectors). The angle of orientation of the in-plane vector relative to the ascending direction y is also reported. The corresponding average values obtained from 2D2C-PIV are also shown (horizontal dashed lines). In Fig. 12 similar profiles are provided first in the central part of the near-wake at $y = 20.8$ mm, then across the wake for $y = -10$ mm, and finally along the line of maximum velocity plotted in yellow color on Fig. 11a. We can first notice that, whatever the position, the z-profiles of the norm and orientation of $\mathbf{V}_{2D}$ reveal a small scattering, even when the norm of $\mathbf{V}_{2D}$ becomes comparable to v_z in the wake (at position $y = -10$ mm). These profiles are symmetrical with z, as expected at least far from the bubble, and the signature of the velocity gradients at the walls is clearly visible for $|\mathbf{V}_{2D}|$. The measurement of the z-component of the velocity is however very noisy. This is the most important limit of our exploration. It is due to the great contrast with the in-plane induced velocities that are far larger, as well as to our choice of a large volume of interest in the (x, y) plane at the expense of the resolution in the z direction.

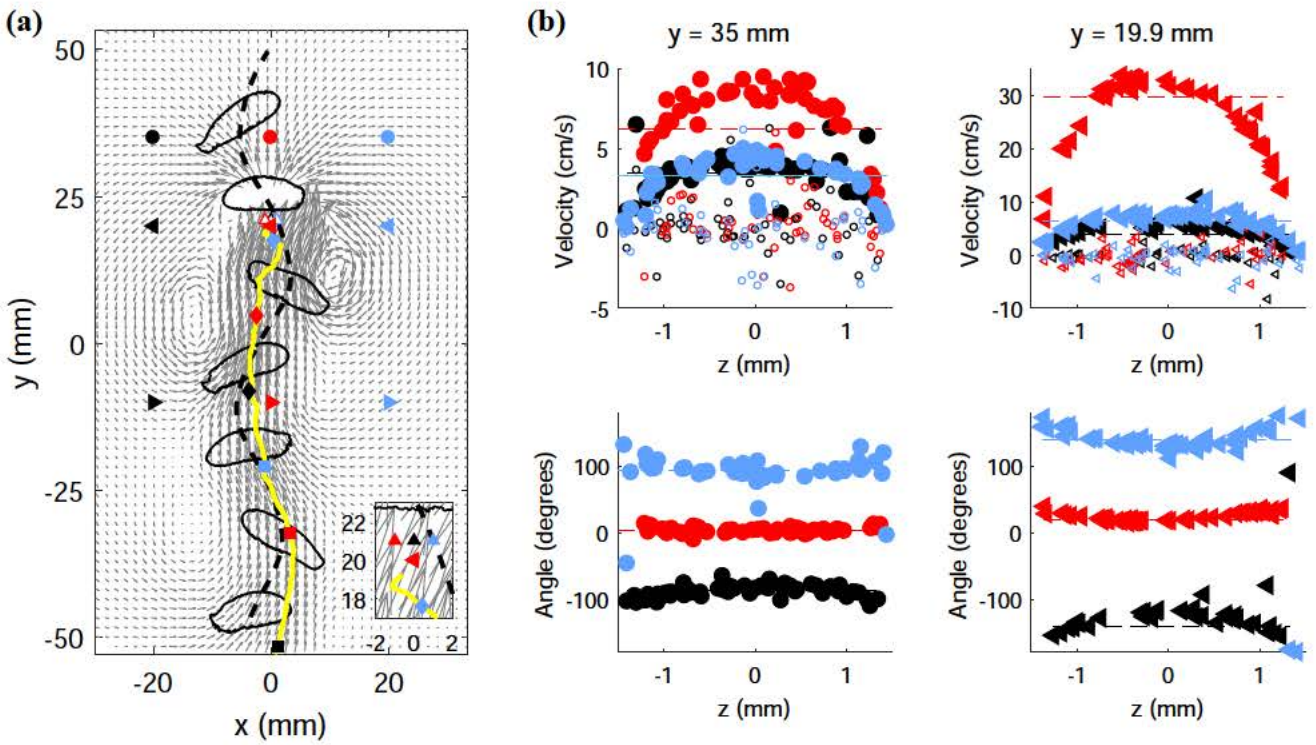

Fig. 11 Velocity profiles measured across the gap at various locations for a given time step corresponding to $t = 0.6$ s. The particles inside squares of side 1.286 mm in the (x, y) plane and for all values of z were considered. The bubble centroid is at $(x, y) = (-1.5, 25.1)$ mm at that instant. **a** Positions where the velocity profiles were measured; the trajectory of the bubble is shown as a dashed line, as well as its contour at regular time intervals $dt = 0.0714$ s in black continuous lines; the yellow line is the line of maximum velocity $x_{v_{max}}(y, t)$ at the same instant. **b** Norm of the in-plane vector (top) and its orientation θ (bottom) as a function of z at various x and y locations; the z-component of the velocity is also plotted with open symbols, despite its great scattering, for comparison; the velocities and orientations obtained at the same regions with the 2D2C-PIV technique from the frontal view of the tomo-reconstructed images are shown as dashed horizontal lines. On the left (respectively right), measurements performed at 3 locations along $y = 35$ mm (respectively, 19.9 mm)

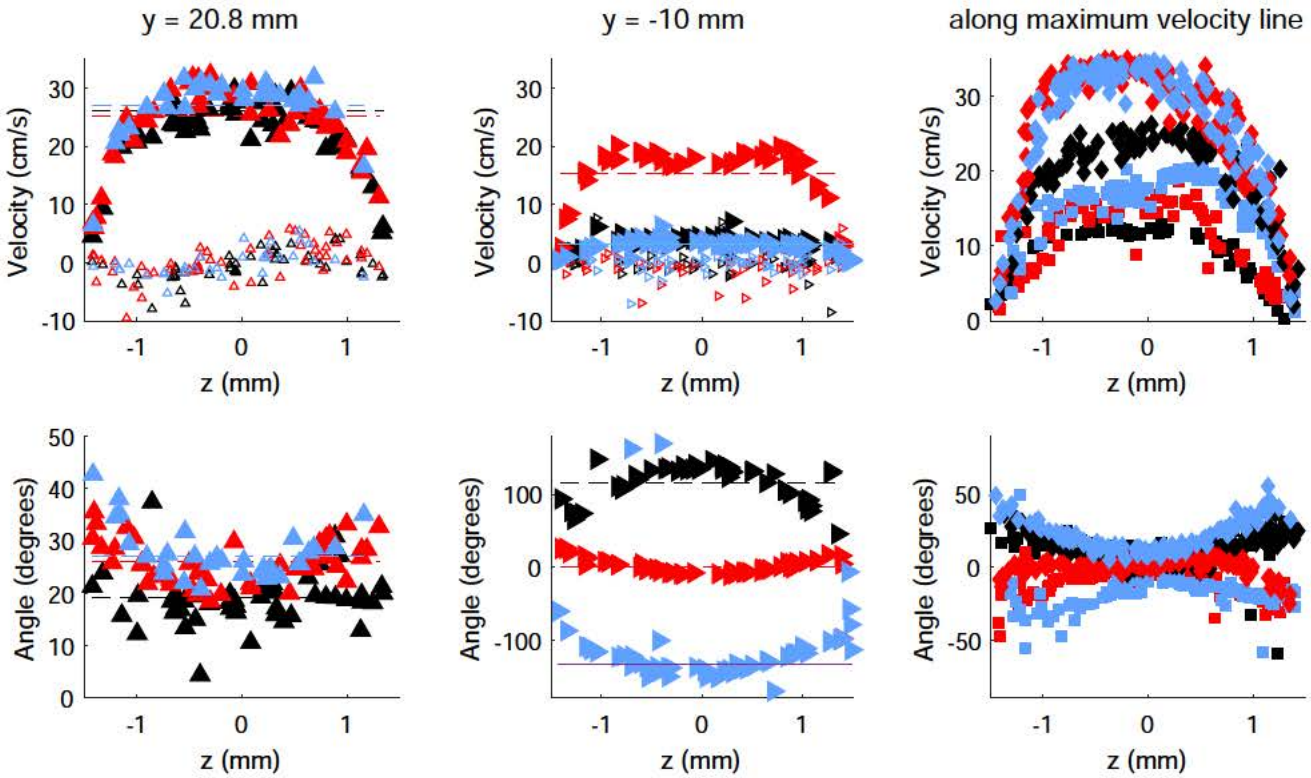

Fig. 12 Velocity profiles measured across the gap at various locations (as in Fig. 11). Left column (resp. central and then right columns) reports measurements performed at 3 locations along $y = 20.8$ mm near $x = 0$ as shown in the insert of Fig. 11-a (respectively $y = -10$ mm, and then along the line of maximum in-plane velocity v_{max}). The dashed horizontal lines in the left and centre columns represent the velocities obtained by applying the 2D2C-PIV technique to the tomo-reconstructed images

The z-component of the velocity is expected to be different from zero in a region close to the bubble. And indeed at $y = 20.8$ mm in the central part of the wake, an anti-symmetrical profile of $v_z(z)$ can be detected that is the signature of a complex three-dimensional vorticity distribution in the near wake (Fig. 12). At larger distances from the bubble the z-component vanishes and cannot be accurately measured.

We now focus our attention on the distribution along the z-axis of the angle characterizing the in-plane velocity orientation. In front of the bubble ($y = 35$ mm) the angle does not significantly depend on z (Fig. 11). However, for the other locations, the orientation of the velocity vector $\mathbf{V}_{2D}$ varies with the in-gap z-position. The angle varies as a response to unsteady re-orientations of the flow induced by the release of vortices in the wake. Due to viscosity, as compared to central layers, the layers near the walls adapt themselves to the impulsion with time delays and changes in amplitude.

A clear vision of the 3D flow emerges. The z-component of the velocity is negligible, and across the z-direction the flow is organized in slices parallel to the plane of the cell with a vector $\mathbf{V}_{2D}$ that varies with z in intensity and also in orientation. A global view of the instantaneous velocity field behind the bubble is provided in Fig. 13 where the vectors are plotted for various positions across the gap. Each vector was calculated as the average velocity of all the particles that lie within parallelepipeds of thickness $\delta z = 0.2$ mm, and centered at different positions in the gap. It can first be noticed that the vector field in the (x, y) plane evolves continuously across the gap. Then, in the ascending wake, whatever the z-position of the slice, the associated velocity vectors do not deviate from each other more than 30°. Conversely, in the vortices there may exist angular deviations up to 90° between the various slices.

The dynamics of the liquid velocity field for different slices along the z-axis are illustrated in Figs. 14 and 15. At first the velocity $\mathbf{V}_{2D}$ at a given position in the (x, y) plane is examined as a function of time (Fig. 14). The norm of $\mathbf{V}_{2D}$ and the angle θ are plotted for 4 slices of thickness $\delta z = 0.2$ mm centered on various z-positions. The in-plane position ($x = 8$ mm, $y = -30$ mm) of observation was selected because it is crossed by an early vortex (number 3 in Fig. 10). The signature of the vortex passage is clear on both the norm and the orientation of the velocity, whatever the considered slice (Fig. 14). But, even if the associated temporal sequences are similar for each slice, they all differ in intensity and in temporal delays. We can notice that, at short times ($t > 0.6$ s) after the passage of the vortex, whatever the z-slice, the value of $|\mathbf{V}_{2D}|$ decreases exponentially

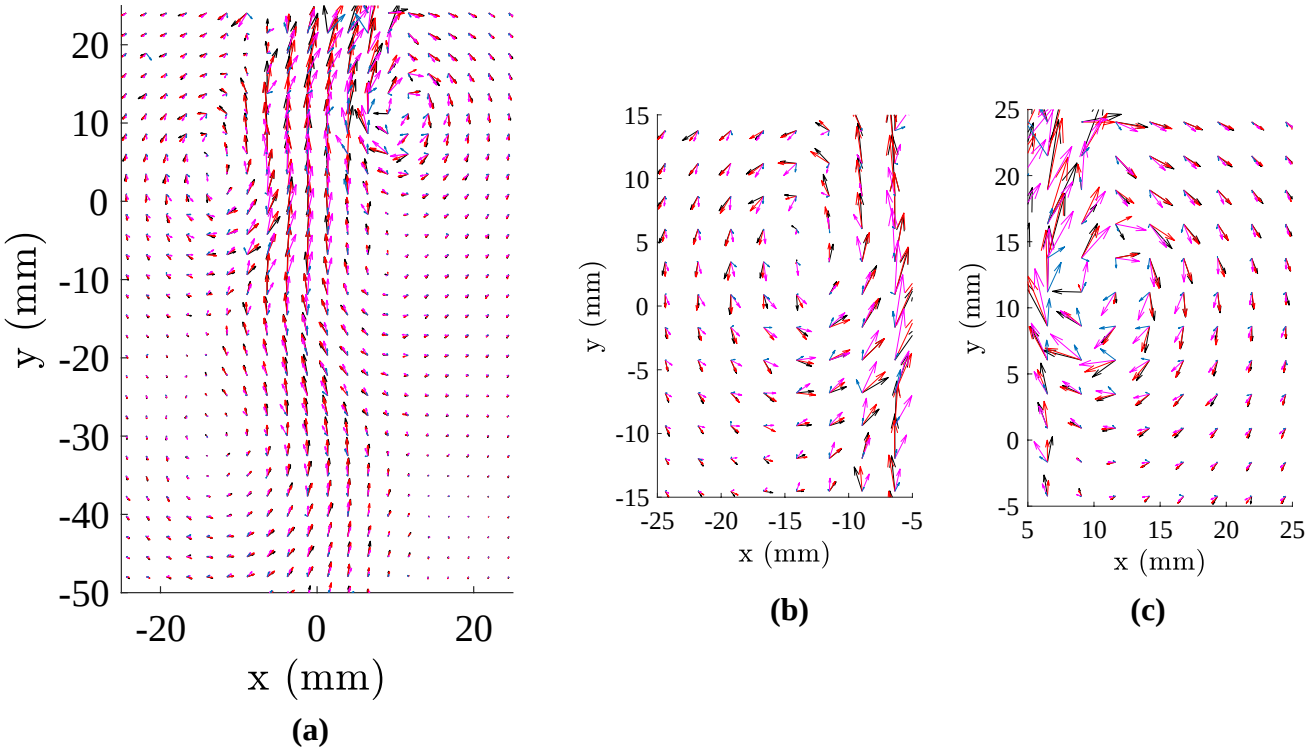

Fig. 13 Superposition of velocity vectors projected on the (x, y) plane for various z positions in the gap ($z = 0$, ± 0.4, ± 1 and ± 1.4 mm for black, red, magenta, and blue-grey colors). The vectors $\mathbf{V}_{2D}(x, y, z, t) = v_x \mathbf{e_x} + v_y \mathbf{e_y}$ are calculated from the STB reprojection at $t = 0.6$ s for slices of thickness $\delta z = 0.2$ mm; symmetric slices with respect to $z = 0$ are averaged. In order to allow visual analysis, only one vector over 8 is plotted. **a** Global view of the wake, **b** and **c** zooms on the vortices

following the scaling law discussed in Filella et al. (2015) for the gap-averaged velocity that behaves as $\exp(-2.5t/\tau)$ (with $\tau = h^2/4\nu$ the viscous time). The velocity near the wall ($z = 1.3$ mm) is, as expected, smaller than the other measurements, but still follows globally the same trend of decrease at large times. Looking at the orientation θ, it appears that the velocity vector changes significantly its orientation during the bubble passage and the generation of a vortex in the vicinity of the point of observation (Fig. 14b). Indeed the temporal sequence corresponding to the strong variation of the angle occurs over the time scales of the bubble passage $\delta t_B = d/V_\infty$ and of the period T of the vortex array. At times larger than 1 or 2 s, the ratio between velocities measured at a given z position and at $z = 0$ mm no longer evolves with time, and the orientations θ of the motions of all the slices also converge to a unique value ($\pm 5^o$). Differential rotation of the slices is thus dampened and the z-profile dampens as a whole.

It is also possible to post-process the velocity data to follow specific events in the flow, slice by slice. The line of maximum velocity introduced in Sect. 4.1.2 was determined for a slice centered in $z = 0$ and is plotted (light blue line) in Fig. 9 for comparison with the results obtained from the gap-averaged PIV or STB methods. A similar behavior is observed, indicating that this characterization of the wake is robust. It is also interesting, in particular, to analyze vortices released in the wake of the bubble that have their axis initially in the z-direction. The idea is to investigate how these large vortices evolve in the z-direction. Again, the volume of investigation was divided into slices of thickness δz and, for each of them, vortex detection and tracking were performed with the same algorithms of post-processing used in Sect. 4.1. The characteristics (trajectories and intensities) of the vortical structures detected for each slice can then be compared, along with those obtained from the gap-averaged velocity field. Vortex number 5 of Fig. 10 is selected for the following detailed discussion. At first, Figs. 15a and b show that, despite data scattering, it is possible to follow the same vortex that is mainly two-dimensional. Indeed, as can be observed in Fig. 15a, the trajectories of the vortical structures detected for each slice are quite similar, with small deviations no larger than 4 mm, which is smaller than the bubble diameter. They also nearly superpose on the path obtained from gap-averaged velocity measurements (plotted in red dots). The deviations between the different paths result from physical distortions of the vortex during its motion. Indeed, for all the vortices numbered 2, 3, 4, 5 and 6 reported in Fig. 10 a general behavior was observed

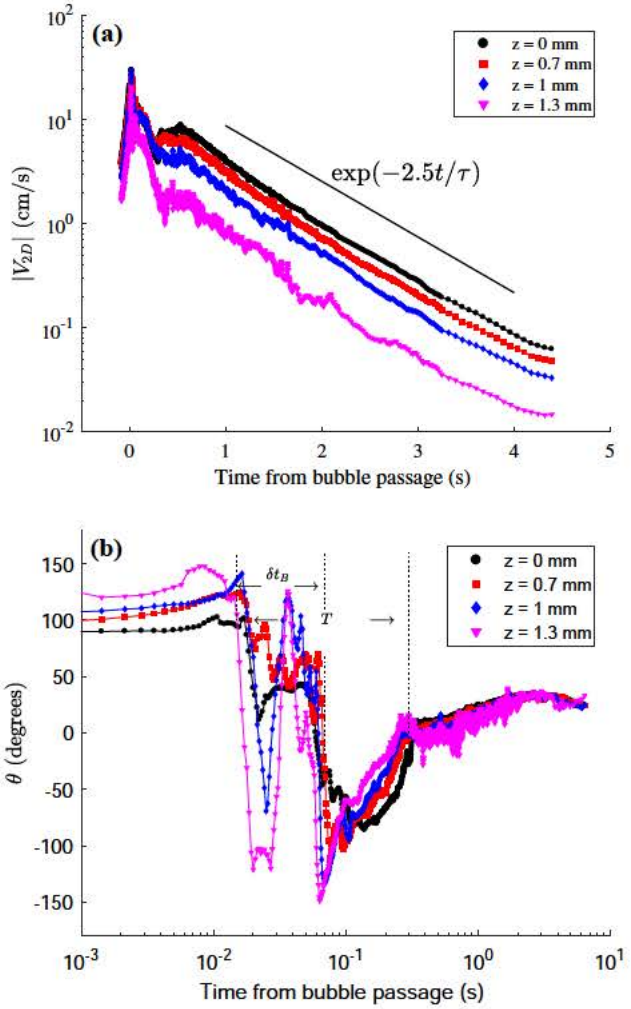

Fig. 14 Temporal evolution of the velocity vectors measured at various in-gap z positions for the fixed in-plane position ($x = 8$ mm, $y = -30$ mm). **a** Norm of $\mathbf{V}_{2D}$, **b** orientation θ of $\mathbf{V}_{2D}$. (The vectors $\mathbf{V}_{2D}(x, y, z, t) = v_x\mathbf{e_x} + v_y\mathbf{e_y}$ were calculated from STB reprojection for various slices of thickness $\delta z = 0.2$ mm centred on the z-positions provided in the legend. We report data averaged for $x \in [7;9]$ mm and $y \in [-31; -29]$ mm)

that is illustrated with vortex 5. During the formation of the vortex and just after its release, a common vortex path is observed for the different measurement positions across the gap. Then deviations appear during about one period and a half after the birth of the considered vortex, that can be related to the formation of the next vortices. This supports the idea proposed by Filella et al. (2015) of the role of vortex interaction on the sharp decay at short times (less than $2T$) of vorticity and velocity (visible in Figs. 14a and 15b), and introduces a three-dimensional component to this effect. In fact, at variance with Benard-von Kármán wake where the released vortices are advected downstream, vortices are here dragged with the trailing flow generated by the bubble. Once a vortex detaches from the bubble, the formation of the next vortices results in the attenuation of its vorticity perpendicular to the plane of the cell (over a time scale T shorter than that associated with viscous friction at the walls). Vortex erosion first occurs as the ascending flow is diverted in favor of the formation of a vortex from the opposite side of the vortex street, and then from the counterflow generated by the co-rotating vortex formed on the same side of the vortex street. In addition to these in-plane mechanisms, we here observe that a significant distortion of the vortex core occurs across the gap when subsequent vortices are formed, which can also contribute to the in-plane vorticity attenuation. Finally, a common path of the vortical structures detected for each slice is recovered at large time. The evolution of the vorticity Ω (in the z-direction) with time also reveals that all the slices present vorticity values that are very similar (Fig. 15b). It can be noticed that the maximum vorticity associated with vortex detachment that occurs at $t \approx 0.55$ s is the same for the central slice (in green color) and when detected from gap-averaged velocity measurements. Near this maximum value, vorticity, nevertheless, becomes more and more intense when the slices are off-centered with $z \leq$ 1mm. For $z = 0.8$ mm or 1 mm this vorticity extremum is here 19% larger than for the gap-averaged velocity measurement. The mechanism for this reinforcement is not clear. Future measurements of vortex sizes might allow to investigate scenario related to possible vortex tube contraction. For slices even closest to the wall, estimation of vorticity—not reported here—is lower than for the other slices or than the value obtained from gap-averaged velocity. For larger times after the vortex release, all the measurements of the vorticity indicate an exponential decay with the viscous time scale $\tau/2.5$ in agreement with Filella et al. (2015). Long time after the passage of the bubble, at a given time t, the vorticity of the slices near the walls is also always smaller than that of the central slice, as the motion is slowed down near the wall. As a conclusion, this investigation of vortex dynamics confirms the release of vortices with large values of vorticity in the z-direction, with intensity and in-plane location that are nevertheless modulated with z-coordinate due to the unsteadiness of the wake.

5 Conclusion

The present exploration by the Shake-the-Box technique of the flow perturbation induced by a bubble rising unsteadily in a thin-gap cell points out several interesting results. At first, despite the strong anisotropy of the volume of observation, it is possible to obtain reliable velocity measurements, provided a precise calibration is achieved. A limitation nevertheless appears due to the great contrast between the in-plane velocity component and that perpendicular to the plane of the cell. This z-component could not be measured

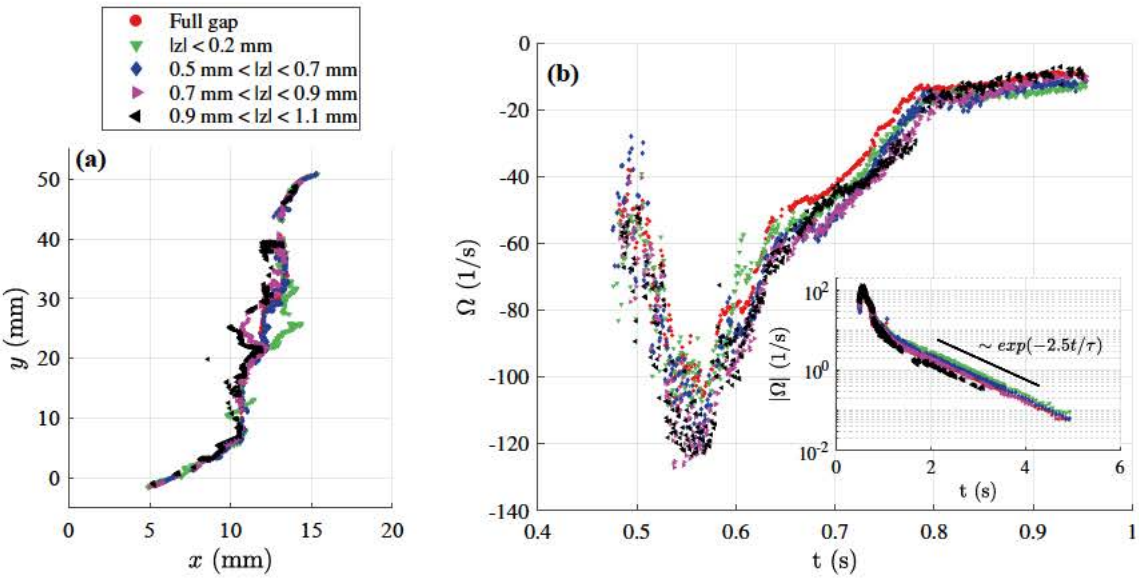

Fig. 15 Vortex evolution at various in-gap z positions. (the z-component of vorticity Ω_z has been calculated from the STB reprojection by a least squares method for various slices of thickness $\delta z = 0.2$ mm centred on the z-positions provided in the legend—except around $z = 0$ mm for which either all the data were considered or a slice with $\delta z = 0.4$ mm. **a** Trajectories of the detected vortices, **b** temporal evolution of the vorticity Ω_z

accurately, while it is non zero in the vicinity of the bubble. However, in the wake of the bubble, the z-dependency of the major x and y-components of the velocity field, has been carefully investigated.

As previous knowledge of the velocity field had been obtained with a 2D2C-PIV technique with volume enlightening (Filella et al. 2015), the present contribution first discussed the gap-averaged velocity field obtained from the STB technique, and meanwhile, presented a direct comparison of 2D2C-PIV and STB technique for this unsteady flow perturbation. 2D2C-PIV was performed on tomo-reconstructed frontal images and measurements of velocity from STB were reprojected on the PIV Eulerian grid. Comparison confirms the consistency of both measurements and the robustness of the characterization of the bubble wake dynamics featuring the line of maximum velocity and the vortex released vorticity as key elements.

The STB technique, however, provides new insights on the variations of the flow within the gap which is impossible to measure with classical optical techniques in such an unsteady confined flow configuration. The instantaneous x and y-components of the velocity are indeed accurately measured, and their dependency upon z is revealed thanks to this novel high-density particle tracking technique. The bubble-induced perturbation generates a flow parallel to the cell plane, at least at a distance greater than one diameter far from the bubble. The velocity profiles in the z-direction show that it consists in a parallel flow with moving slices of varying orientations which all have their own dynamics and strongly evolve in time, but finally follow the general exponential viscous law of decay. The present study has clearly shown that a Poiseuille z-profile does not exist in the flow except at very large time when all velocity vectors across the gap align. The reason for the relative success of recent 2D numerical Volume Of Fluid (VOF) simulations of such bubbles, with momentum equation including a sink term associated to the shear stress at the walls under the assumption of Poiseuille flow (Wang et al. 2014), comes from the introduction of a viscous attenuation term even if the real flow is indeed 3D. The present results could be used to develop other numerical models involving parallel flow hypothesis but keeping the dependency of the velocity on the z-coordinate. The analysis of the released vortices, that were up to now analyzed as having their axis parallel to z-axis, has also revealed that they undergo moderate but non-negligible perturbations of their inclination and vorticity distribution along z-axis that is excited by the releases of the neighboring vortices. This opens new questions about confined wakes dynamics.

Acknowledgements The authors gratefully acknowledge the CNRS Research Federation FERMaT (FR 3089) that gives access to the shared Tomographic PIV 4D system and Toulouse INP that supported, through SMI funding, this collaboration. The authors also thank P. Braud from Institut P' who manufactured the fluorescent particles used in this study, as well as G. Ehses and M. Marchal for their technical support on the experimental set-up.

Compliance with ethical standards

Conflict of interest The authors declare that they have no conflict of interest.

Appendix A: Analytical solution for the unsteady emptying of a vertical planar cell in laminar regime

The velocity profiles during emptying can be obtained by solving the following simplified momentum equation for a viscous incompressible flow far away from any inlet or outlet section.

$$\frac{\partial u}{\partial t} = \frac{(P_0 - P_L)}{\rho L} + \nu \frac{\partial^2 u}{\partial z^2}, \tag{2}$$

where u is the vertical velocity that depends on time t and on z, the coordinate perpendicular to the walls, $\frac{(P_0-P_L)}{\rho L}$ being a constant pressure gradient applied during emptying that ensures the required mass flow rate and ν being the kinematic viscosity. This equation is solved for $0 \leq y \leq h$ and $t > 0$ with the initial condition

$$u(z, 0) = U, \tag{3}$$

with U the front velocity, and the boundary conditions

$$u = 0, \tag{4}$$

whatever $t \geq 0$ at boundaries $z = 0$ and h.

With $U = v_0/12$ and $v_0 = \frac{(P_0-P_L)b^2}{\rho \nu L}$ the solution can be found introducing variables $\eta = z/h$ and $\tau = \nu t/h^2$ by using the method of separation of variables (as in Bird et al. 2002). It can be expressed as

$$\frac{u}{v_0}(\eta, \tau) = \frac{1}{2}\eta(1 - \eta) - \Phi_t(\eta, \tau), \tag{5}$$

with

$$\Phi_t(\eta, \tau) = \sum_{n=1}^{+\infty} D_n \exp(-n^2\pi^2\tau) \sin(n\pi\eta), \tag{6}$$

and

$$D_n = \left(\frac{1}{6n\pi} - \frac{2}{(n\pi)^3}\right)(\cos(n\pi) - 1). \tag{7}$$

References

Adrian RJ, Westerweel J (2011) Particle image velocimetry. Cambridge University Press, Cambridge

Atkinson C, Soria J (2009) An efficient simultaneous reconstruction technique for tomographic particle image velocimetry. Exp Fluids 47(553):553–568

Bessler WF, Littman H (1987) Experimental studies of wakes behind circularly capped bubbles. J Fluid Mech 185:137–151

Bird RB, Stewart WE, Lightfoot EN (2002) Transport phenomena. Wiley, Hoboken

Bush JWM, Eames I (1998) Fluid displacement by high Reynolds number bubble motion in a thin gap. Int J Multiph Flow 24(3):411–430

Collins R (1965a) A simple model of the plane gas bubble in a finite liquid. J Fluid Mech 22(4):763–771

Collins R (1965b) Structure and behaviour of wakes behind two-dimensional air bubbles in water. Chem Eng Sci 20(9):851–853

Discetti S, Natale A, Astarita T (2013) Spatial filtering improved tomographic PIV. Exp Fluids 54(1505):1–13

Elsinga GE, Scarano F, Wieneke B, van Oudheusden BW (2006) Tomographic particle image velocimetry. Exp Fluids 41(6):933–947

Fan LS, Tsuchiya K (1990) Bubble wake dynamics in liquids and liquid–solid suspensions. Butterworth-Heinemann, Oxford

Felis F, Strassl F, Laurini L, Dietrich N, Billet AM, Roig V, Herres-Pawlis S, Loubire K (2019) Using a bio-inspired copper complex to investigate reactive mass transfer around an oxygen bubble rising freely in a thin-gap cell. Chem Eng Sci 207:1256–1269

Filella A, Ern P, Roig V (2015) Oscillatory motion and wake of a bubble rising in a thin-gap cell. J Fluid Mech 778:60–88

Filella A, Ern P, Roig V (2020) Interaction of two oscillating bubbles rising in a thin-gap cell: vertical entrainment and interaction with vortices. J Fluid Mech 888:A13

Graftieaux L, Michard M, Grosjean N (2001) Combining PIV, POD and vortex identification algorithms for the study of unsteady turbulent swirling flows. Meas Sci Technol 12:1422–1429

Hashida M, Hayashi K, Tomiyama A (2019) Rise velocities of single bubbles in a narrow channel between parallel flat plates. Int J Multiph Flow 111:285–293

Hesseling C, Fiedler L, Neal DR, Michaelis D (2019) Volumetric microscopic flow measurement with a stereoscopic micro-PIV system. In: Khler CJ, Hain R, Scharnowski S, Fuchs T (eds) Proceedings of the 13th International Symposium on Particle Image Velocimetry, Institute of Fluid Mechanics and Aerodynamics, Universitt der Bundeswehr Mnchen

Lazarek GM, Littman H (1974) The pressure field due to large circular capped air bubble rising in water. J Fluid Mech 66:673–687

Maas HG, Gruen A, Papantoniou D (1993) Particle tracking velocimetry in three-dimensional flows. Part I: photogrammetric determination of particle coordinates. Exp Fluids 15:133–146

Malik N, Dracos T, Papantoniou D (1993) Particle tracking velocimetry in three-dimensional flows. Part II: particle tracking. Exp Fluids 15:279–294

Piedra S, Ramos E, Herrera JR (2015) Dynamics of two-dimensional bubbles. Phys Rev E 91:063013

Roig V, Roudet M, Risso F, Billet AM (2012) Dynamics of a high-Reynolds-number bubble rising within a thin gap. J Fluid Mech 707:444–466

Roudet M, Billet AM, Risso F, Roig V (2011) Piv with volume lighting in a narrow cell: an efficient method to measure large velocity fields of rapidly varying flows. Exp Therm Fluid Sci 35(6):1030–1037

Roudet M, Billet AM, Cazin S, Risso F, Roig V (2017) Experimental investigation of interfacial mass transfer mechanisms for a confined high-Reynolds-number bubble rising in a thin gap. AIChE J 63(6):2394–2408

Scarano F (2013) Tomographic piv: principles and practice. Meas Sci Technol 24:012001

Schanz D, Gesemann S, Schröder A, Wieneke B, Novara M (2013a) Non-uniform optical transfer functions in particle imaging:

calibration and application to tomographic reconstruction. Meas Sci Technol 24(2):024009
Schanz D, Gesemann S, Schröder A (2016) Shake-the-box: Lagrangian particle tracking at high particle image densities. Exp Fluids 57(5):70
Schanz D, Schröder A, Gesemann S, Michaelis D, Wieneke B (2013b) Shake The Box: A highly efficient and accurate Tomographic Particle Tracking Velocimetry (TOMO-PTV) method using prediction of particle positions. In: 10th International Symposium on Particle Image VelocimetryPIV13, Delft University of Technology
Soloff S, Adrian R, Liu Z (1997) Distortion compensation for generalized stereoscopic particle image velocimetry. Meas Sci Technol 8(12):1441–1454
Wang X, Klaasen B, Degrve J, Blanpain B, Verhaeghe F (2014) Experimental and numerical study of buoyancy-driven single bubble dynamics in a vertical Hele-Shaw cell. Phys Fluids 26(12):123303
Wang X, Klaasen B, Degrve J, Mahulkar A, Heynderickx G, Reyniers MF, Blanpain B, Verhaeghe F (2016) Volume-of-fluid simulations of bubble dynamics in a vertical Hele-Shaw cell. Phys Fluids 28(5):053304
Wieneke B (2008) Volume self-calibration for 3D particle image velocimetry. Exp Fluids 45:549–556
Wieneke B (2013) Iterative reconstruction of volumetric particle distribution. Meas Sci Technol 24(2):024008
Zhang Z, Zhang H, Yuan X, Yu KT (2020) Effective UV-induced fluorescence method for investigating interphase mass transfer of single bubble rising in the Hele-Shaw cell. Ind Eng Chem Res 59(14):6729–6740